Astron. Astrophys. 298, 307–322 (1995)

ASTRONOMY AND ASTROPHYSICS

Specular reflection of sunlight from wavy ocean surfaces and the albedo effect on satellite orbits

I. A statistical model

D. Vokrouhlický [1,2] **and P. Farinella** [3,4]

[1] Astronomical Institute, Charles University, Švédská 8, CZ-15000 Prague 5, Czech Republic
[2] Observatoire de la Côte d'Azur, Dept. CERGA, URA CNRS 1360, Av. N. Copernic, F-06130 Grasse, France
[3] Dipartimento di Matematica, Università di Pisa, Via Buonarroti 2, I-56127 Pisa, Italy
[4] Observatoire de la Côte d'Azur, Dept. Cassini, URA CNRS 1362, B.P. 229, F-06304 Nice, France

Received 14 April 1994 / Accepted 15 November 1994

Abstract. Radiation pressure from sunlight reflected by the Earth's surface and atmosphere affects in a detectable way the orbit of laser–tracked Earth satellites or spacecraft carrying microaccelerometric devices. In particular, long–term perturbations arise as a consequence of radiation specularly reflected from oceans. Most previous models of this effect modelled the ocean surface as a perfectly smooth spherical mirror, such that the reflected light beam is seen at the satellite as collimated and coming from a specific point of the Earth's surface. We now improve on these simplified models, taking into account that the wavy geometry of the water surface results into a finite aperture of the reflected light beam and into an extended (and non–uniform) image of the Sun seen on the surface itself from the satellite's position. First we use geometrical optics and a statistical description of the orientation of small–scale reflecting surface elements to define an averaged Fresnel–type reflection coefficient giving the amount of reflected radiation as a function of incidence angle. Then we compare the results of two possible methods to derive the local radiative field at the satellite: (i) using this averaged reflection coefficient but assuming again a perfectly spherical surface; (ii) analyzing in detail the distribution of ray geometries from the whole region which contributes reflected sunlight, with the method outlined in Vokrouhlický et al. (1993c). The results show that the mirror–like model somewhat overestimates the perturbative effects of reflected sunlight for LAGEOS–type satellites. The extent of this overestimate may range up to about 40%, depending on the assumed statistical properties of the ocean surface geometry, and increases when the effective aperture of the "reflection lobe" is larger.

Key words: celestial mechanics – space probes – radiation mechanisms – Earth

Send offprint requests to: P. Farinella (Pisa address)

1. Introduction

At high levels of accuracy, spacecraft dynamics is complicated by a number of non–gravitational forces which are much more difficult to model than the gravitational ones, and frequently cause subtle long–term effects (Milani et al. 1987; Mignard et al. 1990; Vilhena de Moraes 1994). Among them, we have recently studied in some detail the so–called *albedo effect*, that is radiation pressure caused by sunlight reflected/diffused from the Earth's surface and atmosphere (Lucchesi & Farinella 1992; Vokrouhlický & Sehnal 1993; Vokrouhlický et al. 1993a,b and 1994). A reliable assessment of this force is required by the centimetric accuracy of orbital tracking attained in the late 80's for satellites used in space geodesy and geodynamics, such as LAGEOS.

Actually, some investigators had already been developing complex analytical models for the diffusive part of the Earth–reflected solar radiation, accounting for a distribution of the albedo coefficient on the Earth's surface (Rubincam & Weiss 1986; Borderies & Longaretti 1990). At the same time, however, the need was perceived to generalize such approaches to different physical mechanisms of sunlight reflection, related to the optical properties of the involved surfaces and resulting into an anisotropic distribution of the intensity of light emerging from the Earth surface elements (Anselmo et al. 1983; Barlier et al. 1986; Rubincam et al. 1987; Vokrouhlický et al. 1993a,b). Indeed, Barlier et al. (1986) explicitly proved a theorem stating that the orbit–averaged along–track component of the albedo effect perturbation (resulting into long–term semimajor axis changes) is of the first order in the satellite's orbital eccentricity, provided one accounts only for isotropically reflected (namely, diffused) radiation. However, these authors also showed that the long–term semimajor axis effects of the albedo force — important to assess the origin of the observed orbital residuals in the case of the laser–tracked LAGEOS satellite — are

significantly increased when the non–isotropic or specular part of reflection is taken into account. This was shown by modelling the oceans as simple mirror–like surfaces, partially covered by a variable distribution of diffusive clouds. Later on, similar conclusions were derived from more complex models of non–isotropic reflection from the oceans and/or the clouds (Rubincam et al. 1987; Lucchesi & Farinella 1992; Vokrouhlický & Sehnal 1993; Vokrouhlický et al. 1993a,b). Also, we have recently investigated atmospheric refraction and absorption of sunlight at a global level (i.e., neglecting cloud coverage effects; Vokrouhlický et al. 1994), and have showed that such effects can be modelled to a high accuracy in a fairly simple way.

In this paper, we intend to address an aspect of sunlight reflection by the Earth's oceans that has been neglected so far. To explain our motivations, we recall that the earliest models of the albedo effect (e.g. Levin 1962) did not neglect the specular reflection mode. However, Wyatt (1963) put into question its importance, arguing that favourable conditions for it being significant (sufficiently smooth water surfaces) may exist only on continental lakes. We quote from him:

"Although the oceans cover 71 percent of the globe, it is only very rarely that a patch of ocean is perfectly calm. Nearly always it is wavy and rippled, and the solar image is seen to be smeared out over a rather large angular area. Pure specular reflection is more likely to be experienced over small bodies of water that are less disturbed by the wind. ... However, the increased efficiency of small lakes is offset by the small fraction of the Earth's surface that they occupy. It appears very likely that the secular effect of specular radiation pressure is small."

When specularly reflected radiation was discussed again, starting in the 80's, in connection with the analysis of LAGEOS' orbital residuals (Anselmo et al. 1983; Barlier et al. 1986; Vokrouhlický et al. 1993a,b), these studies did not address Wyatt's objection, since they assumed for the sake of simplicity a mirror–like model of oceanic specular reflection. Thus, the quantitative results obtained in those papers can be seen as questionable. This problem was called to our attention by Slabinski (1993, personal communication).

The basic issue may be stated as follows. According to previous modelling work (Barlier et al. 1986; Vokrouhlický et al. 1993a,b), the importance of specularly reflected sunlight increases for large incidence zenith angles, owing to the relationship between reflection coefficient and incidence angle predicted by Fresnel's law [see Eq. (2) later]. Therefore, one would expect that the perturbation due to specularly reflected sunlight has sharp peaks near the configurations where the satellite "sees" a narrow Earth crescent, and lies near the horizon as viewed from the reflecting Earth surface (Vokrouhlický et al. 1993a,b). However, it is exactly at such configurations that the "roughness" of the oceanic surface should mostly affect the efficiency of reflection, smearing out the region of Earth surface from which nearly–grazing light rays are reflected toward the satellite, and at the same time causing complex multiple reflections between wave crests and troughs. Thus, it could be expected that the occurrence of small–scale waves and ripples may significantly affect the magnitude of the perturbations caused by nearly–tangential reflection of sunlight, and that these perturbations were not estimated in a realistic fashion in the previous studies mentioned earlier.

Our purpose in this paper is that of deriving a quantitative estimate of the effects due to the wavy geometry of ocean surfaces. Basically, we will use just geometrical optics. This is justified by the fact that we deal with the reflection of short–wave (visible) radiation (note, however, that a similar problem has been also discussed for radiation in the radio band, by employing techniques based on the electrodynamics of wave propagation; see Bass & Fuks 1979). First, we shall show that the largest effects of specularly reflected radiation actually do not occur when the satellite is in the part of its orbit just before entry to or after exit from the Earth's shadow, as we assumed in the previous discussion. This is mainly due to the global curvature of the Earth's surface, and also to atmospheric extinction (these mechanisms are discussed in detail in Vokrouhlický et al. 1994). The peaks of the radiation pressure force due to specularly reflected light are thus shifted to solar zenith angles of about 60° or 70°, and in such configurations the influence of surface waves is much decreased.

Then, we shall use some detailed statistical models for the orientation of very small surface elements on the ocean surface, to show that the finite aperture of the "reflection lobe" due to the small–scale surface roughness does indeed result into some decrease of the radiation force caused by specularly reflected sunlight, with respect to the models assuming a collimated, mirror–like reflection. Although the detailed results depend on the adopted model for the sea surface roughness, we shall confirm the finding of Lucchesi & Farinella (1992) that the magnitude of the specular reflection force is not very sensitive to the aperture angle of the reflection lobe, provided this stays small enough. In a forthcoming paper, we shall study in detail how much the more realistic models of oceanic specular reflection developed here may affect the magnitude of long–term perturbations on the orbit of LAGEOS–type satellites, and we shall compare the results with those of Rubincam et al. (1987; later revisited by Lucchesi & Farinella 1992), whose phenomenological approach was based on photometric data obtained by the Nimbus 7 satellite (Taylor & Stowe 1984).

Apart from assessing the reliability of previous models of the albedo effect in the context of LAGEOS orbit analysis, there are other reasons for elaborating new models of specular reflection from ocean surfaces, taking into account their wavy structure in a realistic way. First, data analysis for future microaccelerometric space projects (see e.g. Peřestý & Sehnal 1992) will possibly require such models. Second, the lack of a theoretical understanding of oceanic specular reflection has resulted into inconsistent assessments of this effect in developing the software packages currently used for satellite orbit determination and analysis: for instance, radiation pressure from oceanic reflection has been taken into account by Klinkrad et al. (1990, for the ERS–1 mission) and neglected by Fliegel et al. (1992, for the GPS satellites) and Antreasian (1992, for the TOPEX/POSEIDON mission).

The remainder of this paper is organized as follows. In Sect. 2 we describe our statistical models for the specular reflection from a wavy water surface which on the large scale is on average planar (zero curvature), and discuss a possible way of generalizing the Fresnel reflection law to such a surface. In Sect. 3 we consider specular reflection from the Earth's surface taking into account its finite global curvature, and applying the results obtained in Sect. 2 to a collection of local surface elements of size much smaller than the Earth's radius. In Sect. 4 we apply the results of these models to several specific examples, and in Sect. 5 we summarize the main conclusions of this work.

2. Statistical model for the reflection from a "rough" surface element

In this section we consider specular reflection of a homogeneous radiative field from a "rough" Earth surface element. Our description of the "roughness" property is a statistical one, as follows (see Fig. 1). First, we consider a surface element $\Delta S(\boldsymbol{N})$, with normal unit vector $\boldsymbol{N}$, which is planar on the large scale, but on the small scale consists of a large number of infinitesimal subelements $d\mathbf{S}(\alpha,\beta)$, having normal unit vectors $\boldsymbol{n}(\alpha,\beta)$, where (α,β) are spherical angles in the local coordinate system defined by the direction of $\boldsymbol{N}$ [i.e., $\cos\alpha = \boldsymbol{N}\cdot\boldsymbol{n}(\alpha,\beta)$, the origin of the azimuthal angle β being irrelevant]. Then, we assume that the orientation of the different infinitesimal surfaces follows a probability distribution $\hat{p}(\alpha)$, which is a function of the angle α that gives the tilt of the $\boldsymbol{n}$ direction to the "average local vertical" $\boldsymbol{N}$ and is independent of β. Thus, $p(\alpha)\ \sin\alpha\ d\alpha d\beta \equiv \hat{p}(\alpha)\ d\alpha d\beta$ gives the probability of $\boldsymbol{n}$ being directed in the intervals $(\alpha,\alpha+d\alpha)$ and $(\beta,\beta+d\beta)$. The normalization of $p(\alpha)$ and $\hat{p}(\alpha)$ is provided by the relationship:

$$\int d\alpha d\beta\ \sin\alpha\, p(\alpha) \equiv \int d\alpha d\beta\ \hat{p}(\alpha) = 1 \qquad (1)$$

(note the geometrical factor $\sin\alpha$ providing a kind of weight to the different values of α). We use three different models for the probability distribution $\hat{p}(\alpha)$:

(i) a uniform distribution function $\sin\alpha\, p(\alpha)$ = constant, up to a higher cutoff at $\alpha = \alpha_\star$, $\alpha_\star$ being an input parameter (this will be referred to as *model 1*);

(ii) an exponentially damped distribution function $\sin\alpha\, p(\alpha) = c_1 \exp(-c_2\alpha)$, assumed to hold up to a cutoff $\alpha_\star = 45°$ [$\hat{p}(\alpha) = 0$ for $\alpha > \alpha_\star$], with c_1 providing the normalization constant and c_2 being an input parameter related to the width of the distribution (this will be referred to as *model 2*);

(iii) a simplified version of the Gram–Charlier distribution law derived by Cox & Munk (1954) from aerial photographic data of the sun's glitter on the sea surface (*model 3*):

$$\sin\alpha\, p(\alpha) = \frac{1}{2\pi\sigma^2}\frac{\sin\alpha}{\cos^3\alpha}\exp\left(-\frac{\tan^2\alpha}{2\sigma^2}\right),$$

where the parameter σ (assumed to be equal to both σ_c and σ_u, in Cox and Munk's notations, in such a way that no dependence on β is introduced) is derived from Cox and Munk's formulae for a "clean" sea surface by assuming an average wind speed of about 7 m/s (Wentz et al. 1984), so that the distribution has a maximum for $\alpha = 7°.5$ (and then rapidly drops off). We have also introduced a cutoff at $\alpha_\star = 25°$, consistent with the data quoted by Cox and Munk. Note that we have neglected all but the first (Gaussian–like) term in the Gram–Charlier series, namely we have set to zero all the corresponding "skewness" and "peakedness" coefficients, which is reasonable in view of the data. Similar simplifications have also been used in some recent oceanographic studies (e.g. Hennings et al. 1994).

In all the three cases, β is assumed to take all possible values in the interval $\langle 0, 2\pi\rangle$. The distribution function $\hat{p}(\alpha)$ plays the role of a phenomenological input into our theory. The motivations for our three model choices are as follows: model 1 is just the simplest conceivable one; model 2 bears some similarity to the phenomenological reflection law used by Rubincam et al. (1987) and Lucchesi & Farinella (1992); and model 3 is derived from empirical data, albeit through a number of simplifying assumptions. Comparing the results of the three models will provide information about the sensitivity of the results to the assumptions regarding the statistical properties of sea surface "roughness".

In principle these three models could well be replaced by different ones, based either on new real data on oceanic surface waves or on some hydrodynamical theory of the air–water interactions. Another possibility would be to replace our probabilistic models of the geometrical properties of the ocean surface with some more specific mathematical description — e.g., two–dimensional sine waves, or some other function with a a given Fourier transform. This would allow one to treat in a deterministic way the reflection of light rays from the surface, and possibly also the multiple reflection phenomena. However, in our opinion, our simple models are more suited to the current needs of satellite orbital analysis and determination. Even though they cannot account in an accurate way for multiple reflections and mutual shadowing of waves, we will show at the end of this Section that our method allows us to easily obtain a quantitative estimate of the importance of these effects. Anyway, as we mentioned in Sect. 1, they are most important for a surface–grazing orientation of the light rays, and in this case the perturbing force is much decreased by the global curvature of the ocean surface (see Sects. 3 and 4).

The reflectivity function (fraction of the incident energy flux associated with specularly reflected radiation) for a plane wave of unpolarized incident radiation at the planar boundary between two unmagnetized optical media (air and water in our case) is given by the Fresnel coefficient $\mathscr{R}(\vartheta_0)$:

$$\mathscr{R}(\vartheta_0) = \frac{1}{2}\frac{\sin^2(\vartheta_0-\vartheta_\star)}{\sin^2(\vartheta_0+\vartheta_\star)}\left[1+\frac{\cos^2(\vartheta_0+\vartheta_\star)}{\cos^2(\vartheta_0-\vartheta_\star)}\right] \qquad (2)$$

(see e.g. Stratton 1941; Jackson 1962). Here ϑ_0 is the zenith angle of the incident rays measured from the normal to the considered surface element, and $\vartheta_\star$ is defined by $\varrho\sin\vartheta_0 = \sin\vartheta_\star$, where the constant ϱ depends on the refractive indexes of the

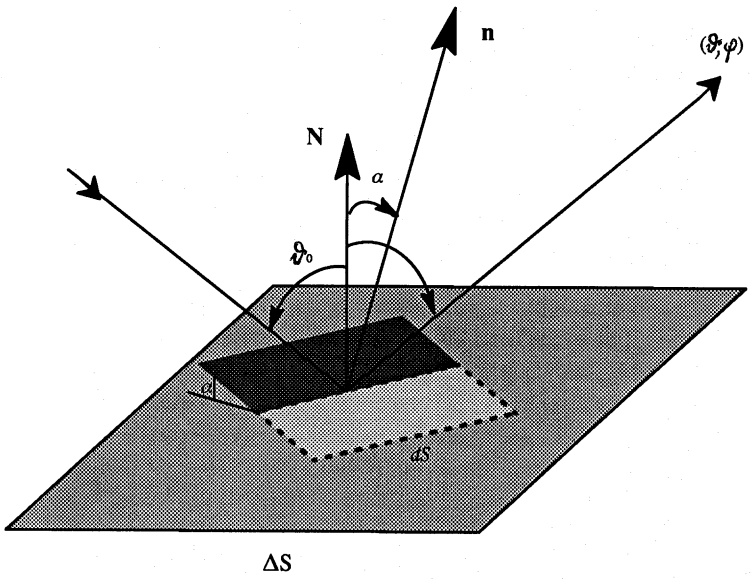

Fig. 1. Polar angles (ϑ, φ) specifying the direction of a ray reflected by a tilted subelement $d\mathbf{S}(\alpha, \beta)$ of an ocean surface element $\Delta S(\boldsymbol{N})$. ϑ_0 is the angle between the direction of the incident ray and $\boldsymbol{N}$

two media; $\varrho = 0.7446$ for an air/water boundary. As we are dealing with a plane wave coming from a given direction (specified by ϑ_0), the Fresnel function also directly determines the ratio between reflected and incident radiative intensities (for the concept of radiative intensity in the current context see Vokrouhlický et al. 1993c).

In our model we assume that ideal specular reflection consistent with Eq. (2) does not apply to the entire surface element $\Delta S(\boldsymbol{N})$, but to the different separate infinitesimal subelements $d\boldsymbol{S}(\alpha, \beta)$. The global reflection from $\Delta S(\boldsymbol{N})$ can thus be seen as the superposition of individual reflections from all the subelements $d\boldsymbol{S}(\alpha, \beta)$, giving rise to a finite lobe pattern of the specular reflection from $\Delta S(\boldsymbol{N})$ instead of a sharp unidirectional beam. It is worth noting that the axial symmetry we assumed for the orientations of the infinitesimal subelements [$p(\alpha)$ does not depend on β] does not entail the consequence that the radiation intensity distribution in the reflection lobe is always symmetrical around its axis (as specified by the ideal specular reflection from ΔS, obtained by assuming $\alpha = 0$). Although the lobe *is* symmetrical when $\vartheta_0 = 0$, for large incidence zenith angles the reflection lobe is significantly elongated in the "vertical" sense (i.e., along ϑ_0). This property is in qualitative agreement with the satellite data discussed by Taylor & Stowe (1984) and consequently also with the model of Rubincam et al. (1987).

We are now going to provide the mathematical formulation of the ideas described above. Together with ϑ_0, the zenith angle of the incident radiation with respect to $\boldsymbol{N}$, we will often use the parameter $\mu_0 = \cos\vartheta_0$. We arbitrarily identify the direction of the incident beam with the negative y–axis of the local system attached to the surface element $\Delta S(\boldsymbol{N})$ (i.e., $\varphi_0 = -\frac{\pi}{2}$). The polar angles (ϑ, φ) give the direction of the beam specularly reflected by the infinitesimal subelement $d\boldsymbol{S}(\alpha, \beta)$ (see Fig. 1). One easily finds the following relationships between the various angular parameters:

$$\cos\vartheta = 2\cos\zeta(\alpha,\beta;\mu_0)\cos\alpha - \mu_0 \,, \tag{3a}$$

$$\sin\vartheta\sin\varphi = 2\cos\zeta(\alpha,\beta;\mu_0)\sin\alpha\sin\beta + \sqrt{1-\mu_0^2} \,, \tag{3b}$$

$$\sin\vartheta\cos\varphi = 2\cos\zeta(\alpha,\beta;\mu_0)\sin\alpha\cos\beta \,, \tag{3c}$$

where $\zeta(\alpha, \beta; \mu_0)$ is the incidence zenith angle measured from the local normal $\boldsymbol{n}(\alpha, \beta)$, given by

$$\cos\zeta = \mu_0\cos\alpha - \sqrt{1-\mu_0^2}\sin\alpha\sin\beta \,. \tag{4}$$

For small tilt angles α it is easy to verify that the reflected beams are close to the "ideal" reflection direction, that is

$$\vartheta - \vartheta_0 = 2\sin\alpha\sin\beta + \mathscr{O}(\alpha^2) \,,$$

$$\varphi - \frac{\pi}{2} = -\frac{2\mu_0}{\sqrt{1-\mu_0^2}}\sin\alpha(\cos\beta - \sin\beta) + \mathscr{O}(\alpha^2) \,.$$

It is important to note than not all the values of (α, β) (i.e., not all the orientations of the subelements) can contribute to the reflected radiation. A necessary condition is that the incoming radiation arrives from above the surface $d\boldsymbol{S}(\alpha, \beta)$, implying $\cos\zeta(\alpha, \beta; \mu_0) > 0$. However, it is easy to see that a sufficient condition is provided by the requirement that the reflected beam lies above the local "average horizon", that is $\cos\vartheta > 0$. Of course, these restrictions on the values of (α, β) apply mainly for large zenith angles of the incident sunlight ($\mu_0 \approx 0$). We shall denote by $\Omega_{\alpha\beta}$ the set of parameters (α, β) which contribute to the reflection lobe; Eqs. (3) imply that the inequality

$$\sin\beta < \frac{\mu_0}{\sqrt{1-\mu_0^2}}\cot(2\alpha) \tag{5}$$

specifies this allowed region $\Omega_{\alpha\beta}$. It is also useful to define $\hat{\Omega}_{\alpha\beta}$ as the set of parameters fulfilling the necessary but not the sufficient condition stated above, that is the relationship

$$\frac{\mu_0}{\sqrt{1-\mu_0^2}}\cot(2\alpha) < \sin\beta < \frac{\mu_0}{\sqrt{1-\mu_0^2}}\cot(\alpha) \,. \tag{6}$$

This just means that the subelements with normals belonging to $\hat{\Omega}_{\alpha\beta}$ are illuminated by incident sunlight but reflect it below the local "average horizon". The corresponding reflected radiation will undergo further reflections from other subelements, and thus can be seen as providing additional incident light with a changed incidence zenith angle:

$$\mu_0 \to \mu_0^{(1)} = \mu_0 - 2\cos\zeta(\alpha,\beta;\mu_0)\cos\alpha \,. \tag{7}$$

The contribution of this secondary reflection process will be discussed later in this Section.

The Fresnel coefficient $\mathscr{R}(\vartheta_0)$ as given by Eq. (2) determines the ratio between the reflected and incident radiative fluxes in the ideal case of a smooth, mirror–like surface. We shall now try to find out a reasonable generalization (an "effective Fresnel coefficient") in the case of the finite reflective lobe discussed earlier. Essentially, we shall just average $\mathscr{R}(\vartheta)$ over the ensemble of infinitesimal subelements $d\boldsymbol{S}(\alpha, \beta)$, with

a given distribution $\hat{p}(\alpha)$. Thinking in terms of the energy flux, one might also introduce an "effective solid angle" spanned by the reflective lobe. We thus propose the following operational definition of the effective (or averaged) Fresnel coefficient $\langle\mathscr{R}\rangle(\vartheta_0)$:

$$\langle\mathscr{R}\rangle(\vartheta_0) = \frac{(\text{ energy passing through the reflection lobe})}{(\text{effective solid angle of the reflection lobe})} \times \frac{1}{(\text{incident energy})} ,$$

which is equivalent to

$$\langle\mathscr{R}\rangle(\vartheta_0) = \frac{\int_{\Omega(\vartheta,\varphi)} d(\cos\vartheta)d\varphi\, \mathscr{R}[\zeta(\vartheta,\varphi)]\, p[\alpha(\vartheta,\varphi)] \left|\frac{\partial(\cos\alpha,\beta)}{\partial(\cos\vartheta,\varphi)}\right|}{\int_{\Omega(\vartheta,\varphi)} d(\cos\vartheta)d\varphi\, p[\alpha(\vartheta,\varphi)] \left|\frac{\partial(\cos\alpha,\beta)}{\partial(\cos\vartheta,\varphi)}\right|}$$

$$= \int_{\Omega(\alpha,\beta)} d(\cos\alpha)d\beta\, \mathscr{R}[\zeta(\alpha,\beta;\mu_0)]\, p(\alpha) , \qquad (8)$$

where $\Omega(\vartheta,\varphi)$ is the set of spherical angles (ϑ,φ) characterizing the subelements contributing to the specular reflection lobe. The denominator of the right–hand side of the upper line of Eq. (8) is just equal to unity due to the normalization (1). Note the Jacobian of the transformation $(\vartheta,\varphi) \leftrightarrows (\alpha,\beta)$ in the integrands of Eq. (8) (upper line), which appears because the probability distribution $\hat{p}(\alpha)$ is defined in the (α,β) space, while in the integrands we need the probability distribution for reflection into the infinitesimal solid angle $d(\cos\vartheta)\,d\varphi$.

It is easy to show that our definition of the effective Fresnel coefficient coincides with $\mathscr{R}(\vartheta_0)$ as given by Eq. (2) in the limit of a quasi–smooth surface (i.e., very narrow reflective lobes):

$$\lim_{\alpha_\star \to 0} \langle\mathscr{R}\rangle(\vartheta_0) = \mathscr{R}(\vartheta_0) \qquad (9)$$

and that this is the case for all model choices of $\hat{p}(\alpha)$.

In Figs. 2 we have plotted the effective Fresnel coefficient $\langle\mathscr{R}\rangle$ vs. the incidence zenith angle ϑ_0 computed in a number of different ways, and compared to the ideal Fresnel function $\mathscr{R}$ (longer–dashed line). For the sake of comparison, besides the curves derived with the three models for $\hat{p}(\alpha)$ (and different parameter choices, labelled 1 and 2), we have also plotted a running average of the ideal Fresnel curve $\mathscr{R}(\vartheta_0)$ over an interval tuned to the parameter choices of the various models (shorter–dashed curve). Note that in both Fig. 2a and 2b the dotted lines labelled 3 represent the results from the "empirical" model 3.

Of course, there are little differences among the various curves for small incidence zenith angles, up to $\vartheta_0 \approx 50°$. On the contrary, significant differences are apparent between the effective Fresnel coefficient defined by Eq. (8) and the ideal Fresnel function $\mathscr{R}$ (and its running averages) for nearly–tangential reflection directions (ϑ_0 close to 90°), where the ideal Fresnel function approaches unity. In general, we can see that this limiting behaviour does really overestimate the real reflectivity of a "rough" reflecting surface, and that the running–average method does not yield a good match to the more physical results from Eq.(8). On the other hand, the differences between the results of the different statistical models for $\hat{p}(\alpha)$ are small, and more important than the detailed shape of the distribution function appears to be (in models 1 and 2) the value of the parameters $\alpha_\star$ and c_2, which specify the average tilt of the small–scale subelements with respect to the local vertical. Note that curve 3, derived from Cox & Munk's (1954) data, is closer to curves 2, corresponding to a higher average roughness of the sea surface.

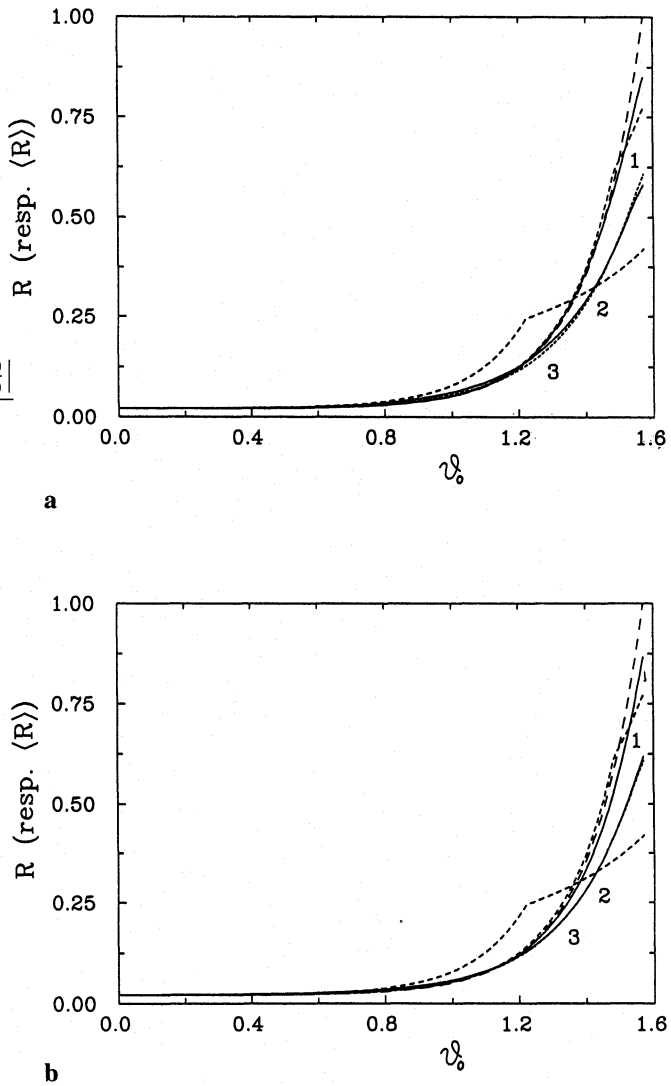

Fig. 2a and b. Effective Fresnel coefficient as defined in the text vs. the zenith angle ϑ_0 (in radians) of the incident sunlight. Parts **a** and **b** correspond to different models (1,3 and 2,3, respectively), for the distribution function $\hat{p}(\alpha)$ of the orientation of the infinitesimal surface subelements. The longer–dashed curves show the ideal Fresnel function (for the mirror–like reflection case). The solid curves show the effective Fresnel coefficients defined by Eq. (8) for two different parameter choices: curves 1 correspond to $\alpha_\star = 5°$ (model 1) and $\ln 2/c_2 = 5°$ [model 2; this implies that $\hat{p}(\alpha)$ decreases by a factor 2 between $\alpha = 0$ and $\alpha = 5°$]; curves 2 correspond to similar choices but with 20° instead of 5° in both cases. The shorter-dashed curves were derived by a running average of $\mathscr{R}(\vartheta_0)$ over an interval of ϑ_0 values of width $2\alpha_\star$ (model 1) or $2\ln 2/c_2$ (model 2). The dotted curves 3 (in Fig. 2b, almost superimposed to solid curve 2) were derived by model 3

We shall now use the method outlined above to derive an approximate estimate of the importance of secondary reflections and mutual shadowing phenomena on the wavy ocean surface. As explained earlier, the rays hitting the infinitesimal subelements with normal directions characterized by (α, β) values in the domain $\hat{\Omega}_{\alpha\beta}$ [see Eq. (6)], after the first reflection are still oriented toward the surface element $\Delta S(\boldsymbol{N})$. Therefore, we shall suppose that they are submitted to a second reflection, with incidence angle given by Eq. (7). Integrating over all the subelements belonging to the $\hat{\Omega}_{\alpha\beta}$ domain, we can estimate the contribution of light rays undergoing secondary reflections to the effective Fresnel coefficient as

$$\delta^{(1)}\langle\mathscr{R}\rangle(\vartheta_0) = \int_{\hat{\Omega}_{\alpha\beta}} d(\cos\alpha)d\beta \left(\begin{array}{c}\text{first}\\ \text{reflection}\end{array}\right)\left\{ p(\alpha)\,\mathscr{R}\left[\zeta(\alpha,\beta;\mu_0)\right] \right. \left(\begin{array}{c}\text{result of the}\\ \text{second reflection}\end{array}\right)\left\{ \langle\mathscr{R}\rangle\left[\arccos\mu_0^{(1)}(\alpha,\beta;\mu_0)\right] \right., \quad (10)$$

where $\langle\mathscr{R}\rangle$ in the integrand is given by Eq. (8).

We have computed the relative importance of $\delta^{(1)}\langle\mathscr{R}\rangle$ with respect to $\langle\mathscr{R}\rangle$ from Eqs. (8) and (10), and then we have plotted the results in Figs. 3 for the three models of the distribution $\hat{p}(\alpha)$. As expected, all the curves show peaks for ϑ approaching 90°, and the peaks are much sharper when the distribution of α is narrower. Note that model 1, which is characterized by a uniform distribution of subelement orientations in the range $(0, \alpha_\star)$, shows a somewhat larger contribution from secondary reflection than model 2 (exponential decay for increasing α values), whereas the "empirical" model 3 provides intermediate results. However, in no case the magnitude of $\delta^{(1)}\langle\mathscr{R}\rangle$ exceeds 7% of $\langle\mathscr{R}\rangle$. Although very approximate, this estimate shows that in the present context a detailed treatment of secondary (and multiple) reflections is not needed. Hereinafter, we are thus going to neglect these phenomena.

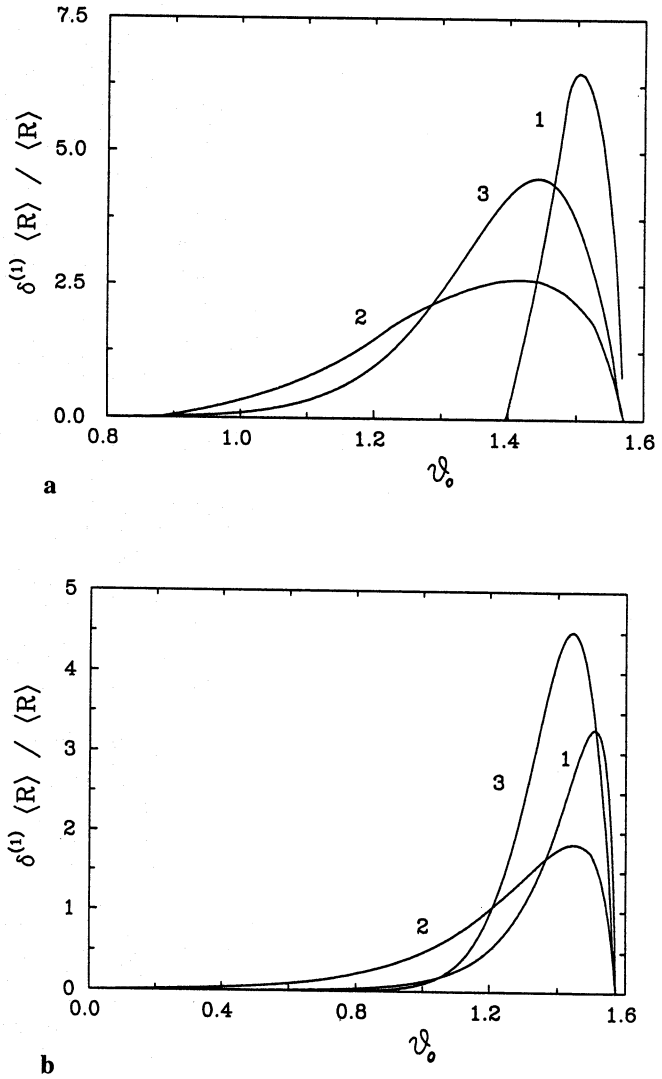

Fig. 3a and b. The ratio $\delta^{(1)}\langle\mathscr{R}\rangle$ (in percent) between the contribution of secondary reflections to the Fresnel coefficient and the single–reflection value $\langle\mathscr{R}\rangle$, plotted vs. the zenith angle of incident sunlight ϑ_0 (in radians). As in Fig. 2, parts **a** and **b** correspond to models 1,3 and 2,3, respectively, for the $\hat{p}(\alpha)$ distribution. Curves labelled 1 and 2 correspond to choosing 5° and 20°, respectively, for the values of the parameters appearing in $\hat{p}(\alpha)$ (models 1 and 2), as explained in the caption of Figs. 2. Curves with label 3 are derived from model 3

3. Reflection from the spherical Earth's surface

In this section, we shall develop a detailed algorithm to compute the radiative force due to specularly reflected solar radiation from the oceans, accounting both for the wave effects and for the global curvature of the Earth's surface, which will be assumed to be spherical.

Let us start with a methodological comment. A possibility for applying in a simple way the approach discussed in Sect. 2 would be that of replacing the "ideal" Fresnel coefficient $\mathscr{R}$ [Eq. (2)] with its averaged version $\langle\mathscr{R}\rangle$ [Eq. (8)] in the formulae for the radiation pressure force due to specularly reflected sunlight [e.g. Barlier et al. 1986, Eq. (10); Vokrouhlický et al. 1993b, Eq. (7)]. However, this approach would account only in part for the phenomena caused by the wavy ocean surface, as one would still assume that specularly reflected light comes to the satellite in a collimated beam from one specific point on the Earth's surface. Therefore, in what follows we will develop a more complex algorithm, based essentially on the geometrical optics technique we applied in our previous papers to a variety of related problems (Vokrouhlický et al. 1993c, 1994). The reader is referred to those papers for a full description of our technique; here, we shall just provide a short summary of it.

The method consists of a detailed calculation of the radiative field that gives rise to radiation pressure on the satellite at its own position. Once this radiative field has been derived, one can compute the radiative flux vector, which in the case of a spherical satellite is directly related to the radiation pressure force (see discussion in Vokrouhlický et al. 1993a). The radiative field is characterized by the angular distribution of the radiative intensity I. We associate with each local direction a given light ray,

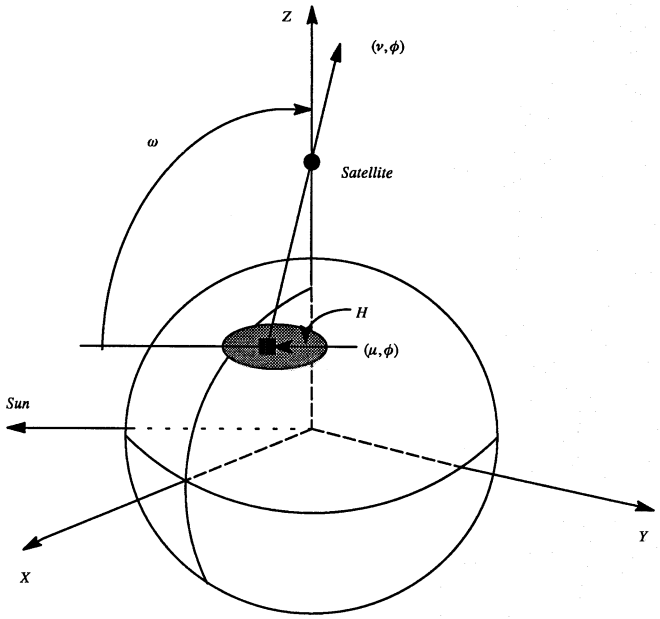

Fig. 4. Reference frames and geometric variables used in the text

and work out how the radiative intensity is "transported" along the rays. Since in the current context we are going to neglect the presence of the Earth's atmosphere (hence of refraction and absorption effects), in general light rays are just represented by straight lines, and the radiative intensity is conserved along any specific ray. Of course, the only exception to this occurs at the point of specular reflection on the ocean surface, where both the ray direction and the radiative intensity are changed discontinuously. Our treatment in the following will thus be devoted to carrying out two tasks: (i) finding out the geometry of the reflected rays in a suitably chosen local reference frame centered at the satellite; (ii) evaluating the radiative intensity for each of the rays contributing to the local radiative field.

3.1. Reference frames

First we define a geocentric satellite–oriented reference frame (x, y, z), such that the z–axis is directed to the satellite and the Sun lies in the xz–plane (the singular case when the Sun and the satellite are aligned does not cause any problem here). We also call ω the geocentric angular distance between the satellite and the Sun. The position of the satellite is thus specified by the unit vector $\boldsymbol{n}_{\rm sat}^{\rm T} = (0, 0, 1)$ and its geocentric distance r. In a similar way, the direction of the Sun is specified by $\boldsymbol{n}_{\rm sun}^{\rm T} = (\sin\omega, 0, \cos\omega)$ and its distance is assumed to be infinite. We thus neglect the angular dimensions of the Sun and approximate its radiation by a homogeneous field with constant intensity I_0 (i.e., by a Dirac delta distribution with respect to the angular variables); this approximation will be discussed later on. We also introduce a system of spherical coordinates (ϑ, φ) in the (x, y, z) frame in the usual way.

We assume that the Earth's surface is spherical, with radius $R_\oplus$. For the sake of simplicity, we also assume in this Section that the Earth's surface is entirely covered by oceans, although this assumption can be easily removed if a realistic model of the ocean/continent distribution is needed (as in Vokrouhlický et al. 1993a,b). Each Earth surface element ($R_\oplus^2 \sin\vartheta\, d\vartheta d\varphi$) is assumed to have the properties described in Sect. 2, namely it is assumed to be "rough" or "wavy" according to some statistical distribution $\hat{p}(\alpha)$. The incident solar radiation is thus specularly reflected into a finite–lobe reflection pattern, rather than in a single direction. As a consequence, there exists in general a finite region $\mathscr{H}$ on the Earth's surface which contributes to the specularly–reflected radiative field at the satellite location (see Fig. 4 for clarifying the geometry). A satellite–centered local frame is obtained from the geocentric satellite–oriented frame by a simple translation along the z–axis, such that the origin coincides with the satellite's position.

Next, we introduce a reference frame attached to the chosen Earth's surface element, characterized by the direction vector $\boldsymbol{n}(\vartheta, \varphi)$ and the polar angles (ϑ, φ). It corresponds to the similar reference frame used in Sect. 2, with the z–axis directed along $\boldsymbol{n}(\vartheta, \varphi)$ and the negative y–axis directed along the projection of the solar direction on the (x, y) plane, normal to $\boldsymbol{n}(\vartheta, \varphi)$. The rotation matrix between the geocentric satellite–oriented frame and the frame attached to the Earth surface element is then easily found. Expressing the unit vector of the satellite's position with respect to the considered Earth surface element both in the geocentric satellite–oriented frame and in the frame attached to the surface element [see Eqs. (3) and (4)] and relating these expressions through the rotation matrix, we obtain the fundamental set of equations

$$2\cos\zeta(\alpha,\beta;\mu_0)\cos\alpha - \mu_0 = (\mu - \xi)\,\sigma \equiv \psi_1 \,, \tag{11a}$$

$$2\cos\zeta(\alpha,\beta;\mu_0)\sin\alpha\sin\beta + \sqrt{1-\mu_0^2} = \frac{\mu\mu_0 - \cos\omega}{\sqrt{1-\mu_0^2}}\,\sigma \equiv \psi_2 \,, \tag{11b}$$

$$2\cos\zeta(\alpha,\beta;\mu_0)\sin\alpha\cos\beta = -\frac{\sin\omega\sqrt{1-\mu^2-\nu^2}}{\sqrt{1-\mu_0^2}}\,\sigma \equiv \psi_3 \,, \tag{11c}$$

with

$$\sigma = \frac{1}{\sqrt{1+\xi^2-2\xi\mu}} \,,$$

where the parameters (μ, ν) are related to the position of the Earth surface element by $\mu = \cos\vartheta$ and $\nu = \sin\vartheta\cos\varphi$; the incidence angle of the solar rays with respect to the local zenith direction μ_0 is given by

$$\mu_0 = \mu\cos\omega + \nu\sin\omega \,; \tag{12}$$

and $\xi = R_\oplus/r$. Usually there exists a unique infinitesimal surface subelement, with normal (α, β), which provides the corresponding reflection. Equations (11) thus describe the geometry of the infinitesimal specular reflection undergone by a particular ray belonging to the radiative field at the satellite's position.

(However, as we shall see later on, more complicated situations may also happen.)

It is easy to check that in the case $\alpha_\star \equiv \max(\alpha) = 0$ (ideal specular reflection from a smooth surface, with no finite–lobe phenomena), Eqs. (11) degenerate to $\nu = \mu$ (or $\varphi = 0$) and

$$\sqrt{1-\mu^2}\sin\omega + \mu\cos\omega = (\mu - \xi)\sigma \ , \tag{13}$$

which may compared for instance with the fourth–degree Eq. (9) in Barlier et al. (1986).

It is useful to solve explicitly Eqs. (11) for the (α, β) parameters, as follows:

$$\cos\alpha = \frac{\psi_1 + \mu_0}{\sqrt{2\left(1 + \mu_0\psi_1 - \sqrt{1-\mu_0^2}\psi_2\right)}} \ , \tag{14a}$$

$$\sin\alpha\cos\beta = \frac{\psi_3}{\sqrt{2\left(1 + \mu_0\psi_1 - \sqrt{1-\mu_0^2}\psi_2\right)}} \ , \tag{14b}$$

$$\sin\alpha\sin\beta = \frac{\psi_2 - \sqrt{1-\mu_0^2}}{\sqrt{2\left(1 + \mu_0\psi_1 - \sqrt{1-\mu_0^2}\psi_2\right)}} \ . \tag{14c}$$

Equations (14) can be combined to express the angle β as

$$\tan\beta = \frac{(1-\mu_0^2)\sigma^{-1} + \cos\omega - \mu\mu_0}{\sin\omega\sqrt{1-\mu^2-\nu^2}} \ . \tag{15}$$

The cosine of the incidence angle μ_0 can be derived from Eqs. (11) as well:

$$\mu_0 = \left(\cos\alpha\sqrt{\lambda} - \mu + \xi\sin^2\alpha\right)\sigma \ , \tag{16}$$

where we have defined

$$\lambda = \xi\left[2\mu - \xi\left(1 + \sin^2\alpha\right)\right] + 2\left(1 + \sigma\cos\omega\right)\sigma^{-2} \ . \tag{17}$$

3.2. Characterization of the specularly reflecting domain on the Earth's surface

Here we shall carry out the first step mentioned earlier, namely we shall characterize the geometry of the region where the radiative field does not vanish in the satellite–centered local reference frame. We introduce a system of polar coordinates (θ, ϕ) in the satellite–centered system, with $\eta = \cos\theta$. One easily finds the relationship between the parameters (η, ϕ), specifying a given light ray in the satellite–centered system, and the parameters (μ, φ) of the Earth surface element from which the light ray is reflected. Besides the trivial relation $\phi = \varphi$, we find

$$\eta = \frac{1 - \xi\mu}{\sqrt{1 + \xi^2 - 2\xi\mu}} \ ,$$

$$\mu = \frac{1}{\xi}\left[1 - \eta^2 + \eta\sqrt{\eta^2 + \xi^2 - 1}\right] \ . \tag{18}$$

Through Eqs. (18), the characterization of the radiative field in the satellite–centered frame is equivalent to the characterization of the specularly reflecting domain $\mathscr{H}$ on the Earth's surface. We shall summarize the algorithm for the determination of its boundary ($\partial\mathscr{H}$), because its image essentially specifies the finite region within which the radiative field does not vanish in the satellite–centered frame. Most of the material of this subsection is based on simple geometrical considerations, plus the use of Eqs. (11). Therefore we just give the results, and the reader is encouraged to verify herself/himself the following equations.

First, note that there are three possibilities concerning the relative position of the domain $\mathscr{H}$, the subsatellite point on the Earth's surface (the pole $\theta = 0$) and the terminator of the region visible from the satellite (given by $\mu = \xi$):

1. $\omega < 2\alpha_\star$: in this case the domain $\mathscr{H}$ contains the subsatellite point; actually, we can also distinguish between subcase (1a), when the subsolar point also lies in the $\mathscr{H}$ domain, corresponding to $\omega < 2\alpha_\star - \arcsin\left[\xi\sin(2\alpha_\star)\right]$, and subcase (1b), when this is not the case, i.e. $2\alpha_\star - \arcsin\left[\xi\sin(2\alpha_\star)\right] < \omega < 2\alpha_\star$.
2. $2\alpha_\star < \omega < [\arccos(-\sqrt{1-\xi^2}) - 2\alpha_\star]$ (provided this is possible, see below): the domain $\mathscr{H}$ neither includes the subsatellite point nor intersects the terminator of visibility;
3. $[\arccos(-\sqrt{1-\xi^2}) - 2\alpha_\star] < \omega < \arccos(-\sqrt{1-\xi^2})$: the domain $\mathscr{H}$ intersects the terminator of visibility.

We shall assume that all the three cases may actually occur. This of course depends on the actual values of the parameters $\alpha_\star$ and ξ (recall that $\alpha_\star$ can be changed within model 1 for the $\hat{p}(\alpha)$ probability distribution, whereas it is fixed to 45° in model 2). For the orbit of the LAGEOS satellite, mentioned in Sect. 1 and further discussed in Sect. 4, the requirement is that $\alpha_\star < 22°.5$, a fairly reasonable assumption. However, it should be noted that the situation when case (2) is not possible (that is, the domain $\mathscr{H}$ still contains the subsatellite point and already intersects the terminator of visibility), occurring for larger values of the $\alpha_\star$ parameter, is only a trivial variation of what will be obtained in the following, thus we shall skip a detailed discussion of it.

In case (1), all the φ values are allowed for the points belonging to the $\partial\mathscr{H}$ boundary. Once the angle φ is chosen, one can determine the corresponding μ parameter (or equivalently ϑ) from Eq. (14a), by fixing $\alpha = \alpha_\star$. The resulting equation has to be solved iteratively. It can be proven that there are just two roots in the relevant interval $\mu \in \langle\xi, 1\rangle$, corresponding to the two points with parameters φ and $\varphi + \pi$.

In case (2), the same procedure can be used again for finding μ once the coordinate φ is given. However, it is evident that now φ is limited to some interval $\langle -\varphi_{\max}, \varphi_{\max}\rangle$, and the two μ roots are to be interpreted as two roots on the same "φ–slice". One easily finds that the $\varphi_{\max}$–slice tangent to the $\mathscr{H}$ domain can be identified by solving the equation

$$\left(1-\mu^2\right)\frac{\partial\mu_0(\mu;\alpha_\star)}{\partial\mu} = \cos\omega - \mu\mu_0 \ , \tag{19}$$

where Eqs. (16) – (17) are used to obtain μ_0 as a function of μ, which plays the role of parameter for the points of the $\partial\mathscr{H}$ boundary. This equation cannot be reduced to a low–degree polynomial equation and has to be solved iteratively for $\mu_{\max}$.

The corresponding angle $\varphi_{\max}$ is then easily determined from Eq. (12).

In case (3), one has to determine the intersection with the visibility terminator. This provides the value of μ such that $\mu_{cr} = \xi$. Using Eq. (14a), one can find the corresponding value of φ_{cr} at the terminator crossing (simultaneously fixing $\alpha = \alpha_\star$).

Note that all the points of the $\mathscr{H}$ domain should satisfy the condition of being illuminated by the Sun (i.e., their angular distance from the Sun should be $\leq 90°$). This condition does not involve any restriction on the construction of the $\partial\mathscr{H}$ boundary in the first two cases discussed above. It can however be shown that for

$$\omega > \frac{\pi}{2} + \arccos\left(\xi\cos^2\alpha_\star + \sin\alpha_\star\sqrt{1-\xi^2\cos^2\alpha_\star}\right) \qquad (20)$$

a portion of the $\partial\mathscr{H}$ boundary exceeds this maximum angular distance from the Sun. This completes what is needed to determine the boundary of the domain $\mathscr{H}$ in all the considered cases.

3.3. Determination of the radiative intensity carried by a specified light ray

We shall now outline our method for the determination of the radiative intensity carried by a light ray in the radiative field characterized in Sect. 3.2. Let us consider a light ray, locally identified by its spherical coordinates (η, ϕ), which is reflected at some point of the domain $\mathscr{H}$. First, we can easily find the location of the reflecting point by using $\varphi = \phi$ and one of Eqs. (18). Once we have found the (ϑ, φ) [or equivalently (μ, ν)] parameters of the reflecting point, we can use Eqs. (14) and/or (15) to determine the parameters (α, β). The zenith incidence angle ζ with respect to the reflecting surface subelement [characterized by the spherical coordinates (α, β) of its normal vector in the local frame attached to the Earth surface element] is easily obtained by Eq. (4). In the formula for the radiative intensity transported along the chosen light ray, we expect to find the intensity at the source I_0 multiplied times the non–averaged Fresnel function $\mathscr{R}(\vartheta)$, giving the fraction of the incident light reflected by the subelement (we use the non–averaged Fresnel function here because we suppose that ideal specular reflection occurs at the subelement). Then, when the integration is carried out over all the subelements forming a given surface element, the weight function $\hat{p}(\alpha)$ must be used to account for the probability of the orientation of the subelements.

Before going on, it must be emphasized that only a part of the effect of the curvature of the Earth's surface has been taken into account so far. On the one hand, we have partially included it by deriving the ray geometry. However, Vokrouhlický et al. (1994) have shown that only a more complete model with the Sun treated as an extended source of radiation can account in a correct way for the effects of the Earth's surface curvature on the reflected sunlight. Roughly speaking, the reason is that a spherical mirror causes a "dilution" of the energy flux coming from an extended source when it is reflected from its surface and then impinges on an external object (in our case, the satellite). But we have used here a simple homogeneous model for the solar radiative field. To correct the corresponding error, which may become quite significant, Wyatt (1963) and independently Barlier et al. (1986) introduced a suitable "dilution factor", whose accuracy has been verified in detail by Vokrouhlický et al. (1994). Thus, we have to introduce in the radiative intensity this additional "dilution factor" $\Psi(\zeta, \xi_\alpha)$ [$J(\theta)$ in the terminology of Barlier et al.], which can be expressed as

$$\Psi(\zeta, \xi_\alpha) = \xi_\alpha^2 \frac{\sin\zeta\cos\zeta}{\sin\rho\,[2\cos(2\zeta-\rho) - \xi_\alpha\cos\rho]}\,, \qquad (21)$$

where we have defined

$$\rho = 2\zeta - \arcsin(\xi_\alpha\sin\zeta)\,,$$
$$\xi_\alpha = \xi\frac{\cos\alpha}{\sqrt{1-\xi^2\sin^2\alpha}}\,. \qquad (22)$$

Actually, we generalized the expressions of the dilution factor derived by Wyatt and Barlier et al. to include the case of subelements with $\alpha \neq 0$, which are not geometrically tangent to the globally spherical surface of the planet.

The expression for the radiative intensity $I(\eta, \phi)$ carried along the considered light ray is thus:

$$I(\eta, \phi) = I_0\,\mathscr{R}(\zeta)\Psi(\zeta, \xi_\alpha)\,, \qquad (23)$$

and the perturbing acceleration on the satellite due to Earth–reflected radiation pressure is given by:

$$\boldsymbol{a} = \frac{\pi R_{sat}^2\,\mathscr{C}_R}{mc}\int_{(\eta,\phi)} d\eta d\phi\, I(\eta,\phi)\hat{p}(\alpha)\left|\frac{\partial(\alpha,\beta)}{\partial(\eta,\phi)}\right|\boldsymbol{n}(\eta,\phi) \qquad (24)$$

(see e.g. Vokrouhlický et al. 1993a). Here $\boldsymbol{n}(\eta, \phi)$ is a unit vector with components $\boldsymbol{n}(\eta,\phi)^{\mathrm{T}} = (\sin\theta\cos\phi, \sin\theta\sin\phi, \cos\theta)$, and the constant appearing before the integral contains the radius (R_{sat}) and mass (m) of the satellite, assumed to be spherical, the velocity of light (c) and the dimensionless coefficient $\mathscr{C}_R$, depending on the properties of the satellite's surface. The integration in Eq. (24) is performed over the set of directions for which the radiative field in the satellite–centered frame does not vanish. This coincides with the image "seen" by the satellite of the domain $\mathscr{H}$, as discussed in Sect. 3.2. Note the appearance of the Jacobian of the transformation $(\alpha, \beta) \leftrightarrows (\eta, \phi)$ in the integrand of Eq. (24), that comes from the fact that $\hat{p}(\alpha)$ is the probability distribution in the (α, β) space, while the integration is performed in the local frame coordinates (η, ϕ). The evaluation of this Jacobian is a straightforward but cumbersome exercise, where Eqs. (11) and (14) have to be exploited. We shall skip the explicit calculations here. Note, however, that singularities in the Jacobian may cause numerical problems in evaluating the integral appearing in Eq. (24), although of course the integral is always convergent. On the other hand, as we already mentioned (see also Sect. 4), when the geocentric position vector of the satellite approaches the sun's direction, the transformation $(\alpha, \beta) \leftrightarrows (\eta, \phi)$ is no more one–to–one, and as a consequence the model yields a spurious decrease of the perturbing acceleration.

It might be argued that the y–component of the satellite acceleration (24), when expressed in the satellite–centered frame, should vanish for symmetry reasons (the Sun lies by definition in the xz–plane). However, this is not true any more when one takes into account the real ocean/continent distribution on the Earth's surface. Actually, in Sect. 3.2 we studied the domain $\mathscr{H}$ from the geometrical point of view only. In a realistic simulation, one should check whether all the points belonging to the geometrically derived domain $\mathscr{H}$ correspond to ocean surfaces, and if not take into account the real coastal lines.

4. Applications

In this section we shall apply our specular reflection theory to the case of the LAGEOS satellite. This choice is motivated by the long–standing effort to understand the long–term orbital residuals of LAGEOS (see Sect. 1) and by our desire to assess how much our previous results on this problem have been affected by the fact of neglecting the wavy geometry of ocean surfaces. In fact, previous studies (Barlier et al. 1986; Vokrouhlický et al. 1993b) have addressed the role of Earth–reflected radiation in generating significant long–term perturbations on LAGEOS, but adopted idealized (mirror–like) specular reflection models for the oceans. Here we shall investigate the behaviour of our more realistic models of oceanic reflection for varying geometries along one revolution of the satellite, whereas a forthcoming paper will be devoted to reinvestigating the long–term effects. Although our examples will thus be restricted to LAGEOS–type orbits, we stress that the same study may be performed for any other satellite orbit (see e.g. the feasibility study for the low–orbiting microaccelerometric experiment MACEK prepared at the Ondřejov Observatory, Vokrouhlický 1994).

In our examples we are not going to use the real LAGEOS orbit, but we will modify the angular orbital elements (the inclination, longitude of the ascending node and argument of perigee) so that extremal configurations are reached, in which the magnitude of the resulting perturbations is maximized. This method has been widely used in previous work on similar issues (e.g. Rubincam et al. 1987; Lucchesi & Farinella 1992), in order to obtain a simple assessment of whether a given source of perturbation is significant with respect to the observed residuals. Also, this allows one to analyse the perturbative effects freed of additional geometrical imprints.

As a first example, we assume that the Sun lies on the equator, the satellite's orbit is equatorial (zero inclination), and the perigee direction (from which the mean anomaly used in the following figures is measured) coincides with that of the subsolar point. Moreover, we assume that the Earth's surface is entirely covered by oceans (a realistic distribution of the continents will be used in the forthcoming study of long–term effects). Note that for a uniform Earth surface the symmetry of the assumed Earth–Sun–orbit configuration implies that the behaviour of the perturbing force along the orbit is in fact independent of inclination, so in this particular case the results apply as well to LAGEOS' real inclination (about 110°).

Fig. 5 displays a sequence of solar image boundaries $\partial\mathscr{H}$ for different Sun–satellite angular distances ω, as seen from the satellite's position (these plots can be obtained by simple transformation formulae from the results of the procedure explained in Sect. 3.2). We have chosen $\alpha_\star = 5°$ here. The first solar image a) corresponds to the perigee position, with $\omega = 0$, and of course it is circular. Its angular radius $\theta_{\rm rim}$, measured in the satellite–centered reference frame, can be determined through the system of transcendent equations

$$\sin(2\alpha_\star - 2\vartheta) = \xi \sin(2\alpha_\star - \vartheta) \ ,$$
$$\theta_{\rm rim} = \arccos\left[\frac{1-\xi\cos\vartheta}{\sqrt{1+\xi^2-2\xi\cos\vartheta}}\right] \ . \qquad (25)$$

For $\alpha_\star = 5°$, one gets $\theta_{\rm rim} = 3°.5$. The small asterisks in the images show the position of the point from which mirror–like specular reflection would be expected to come for a perfectly smooth ocean surface (as used in the previous studies on the subject). As ω is increased [images b) to f)], the the shape of the reflected solar image is deformed and becomes smaller and smaller. There is a factor 2.7 in scale between images a-b) and c-d) and a factor 5 between images a-b) and e-f). This strong apparent shrinking of the solar image is due to two different effects: along θ, the major role is played by the global convex shape of the Earth (namely, it is a geometrical optics effect resulting from reflection into a spherical mirror), whereas along ϕ the reflection lobe would be compressed even for a (roughly) plane reflecting surface, as discussed in Sect. 2. The last two images e–f) correspond to case (3) according to the classification of Sect. 3.2, with the boundary $\partial\mathscr{H}$ intersecting the horizon of visibility (dashed lines in Fig. 5). In case f), moreover, the solar image is partially "cut" as a consequence of the solar illumination requirement, also discussed in Sect. 3.2. We stress that Fig. 5 just shows the $\partial\mathscr{H}$ boundaries of the solar image, but does not provide information about the brightness distribution inside it; in general, the brightness is not uniform, but increases toward the centre of the image itself.

Figs. 6 and 7 show the variation of the radial (S) and transverse (T) components of the radiative force due to specularly reflected radiation along half of the portion of the satellite's orbit lying outside the Earth's shadow (the other half is symmetrical). A number of different models and parameter choices have been used to derive the different curves. As in Figs. 2 and 3, parts a) and b) compare models 1,3 and 2,3, respectively, for the $\hat{p}(\alpha)$ distribution (see Sect. 2); curves labelled 1 and 2 correspond to different parameter choices ($\alpha_\star = 5°$ and 20°, respectively, in model 1 and the same values for $\ln 2/c_2$ in model 2), whereas the dotted curve labelled 3 has been derived with the "empirical" model 3. In all plots, the longer–dashed curve was derived from the simple approach used in previous studies, that is assuming mirror–type reflection from a smooth ocean surface and the "ideal" Fresnel coefficient $\mathscr{R}(\vartheta_0)$ given by Eq. (2) — this should be compared e.g. with Fig. 6a in Vokrouhlický et al. (1994). On the other hand, the shorter–dashed curves correspond to a similar method, but replacing the ideal Fresnel function coefficient $\mathscr{R}(\vartheta_0)$ with the averaged version of it, $\langle\mathscr{R}\rangle(\vartheta_0)$, as

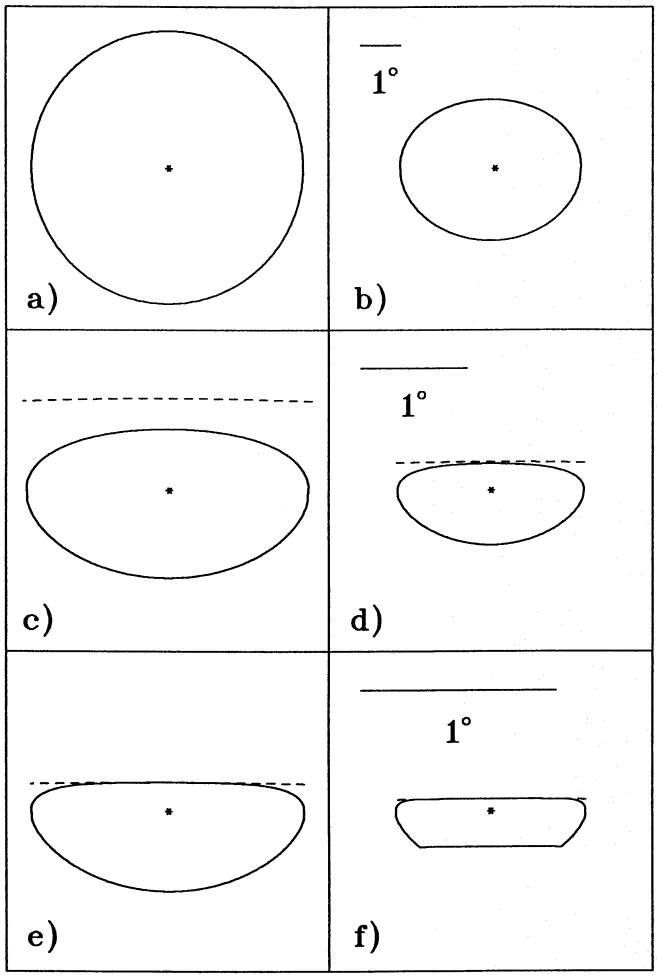

Fig. 5a–f. Different phases of the solar image boundary $\partial\mathscr{H}$ seen from the satellite on the ocean surface. The Sun–satellite angular distance ω is changed along the sequence. The asterisks inside the images mark the points yielding mirror–like specular reflection on an ideally smooth ocean surface. The dashed lines show the position of the Earth's horizon as seen from the satellite. The circular image **a** corresponds to $\omega = 0$, and in the following images ω increases as follows: $\omega = 90°$ for **b**; 124°.1 for **c**; 134°.9 for **d**; 138°.5 for **e**; 142°.1 for **f**. The last value is close to the limit value $\omega_{\rm lim} = \arccos\left[-(1-\xi^2)^{1/2}\right] = 146°.5$, characterizing the sunset as seen from the satellite. As shown by the 1° horizontal bars in **b**, **d** and **f**, the scale is increased by a factor 2.7 passing from images a-b) to c-d) and by a factor 5 passing from **a-b** to **e-f**

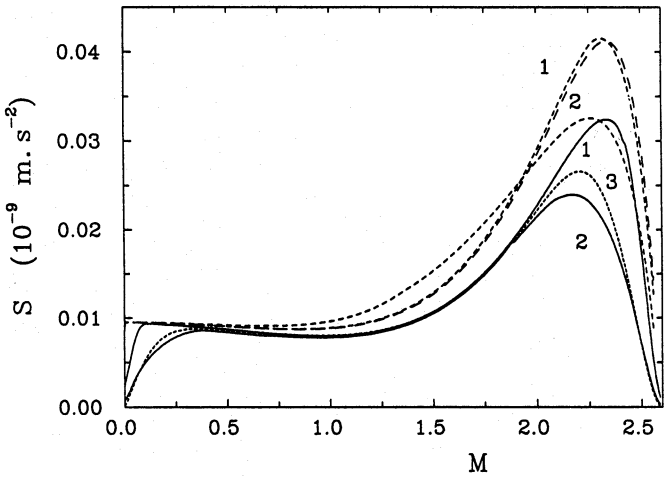

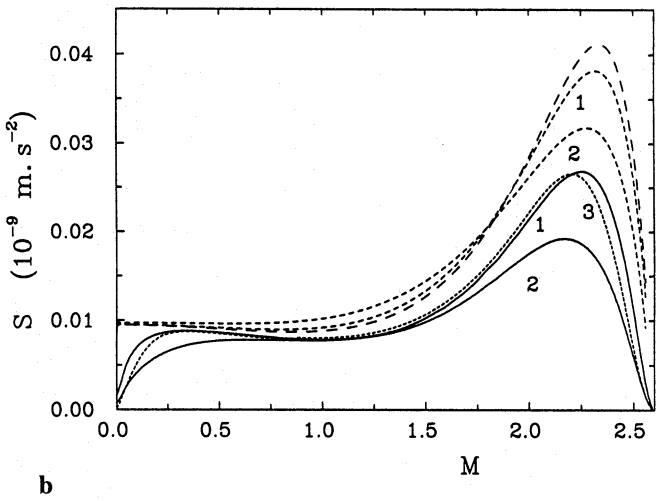

Fig. 6a and b. Radial component S of the radiation pressure acceleration due to specular reflection from the oceans vs. orbital mean anomaly M (in radians, measured from the subsolar point). The chosen orbital configuration is explained in the text. Parts **a** and **b** of the figure correspond to different models (1,3 and 2,3, respectively) for the ocean roughness probability distribution $\hat{p}(\alpha)$. The longer–dashed curves correspond to a smooth–ocean model yielding mirror–like reflection, while the shorter–dashed curves were derived with the simple approach of using just the effective (averaged) Fresnel coefficient (8) instead of the smooth–water one (2). The solid and dotted curves were derived from the full theory developed in Sect. 3. Curves labelled 1 and 2 correspond to the values 5° and 20°, respectively, for the parameters appearing in $\hat{p}(\alpha)$, as explained in the caption to Figs. 2; the dotted curve 3 in both **a** and **b** has been derived by model 3

derived in Sect. 2. Note that in this way we still keep the same geometry of the reflected beam as in the smooth–ocean case, and just change the intensity of it. Of course, the two methods give results closer to each other when the probability distribution is narrow (curves 1) than when a broader range of tilts of the surface subelements is allowed for (curves 2).

Finally, the solid and dotted curves have been derived from our more detailed model taking into account the geometry of reflected rays, as developed in Sect. 3 (labels 1 and 2 still refer to different parameter choices for $\alpha_\star$ and c_2, while label 3 is attached to curves derived with Cox' and Munk's empirical model 3). The most remarkable feature is that both the S and the T curves from the detailed model show a significant decrease in the region near their peak (some 25% in model 1 and 40% in model 2) with respect to curves from the averaged–$\mathscr{R}$ models, and the difference reaches up to a factor ≈ 2 with respect to the mirror–like reflection model. The empirical model 3 behaves in a way similar to models 1 and 2, and it actually closest to

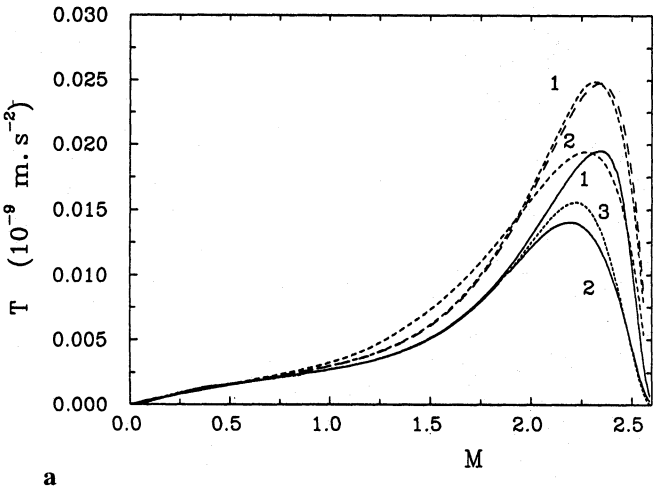

a

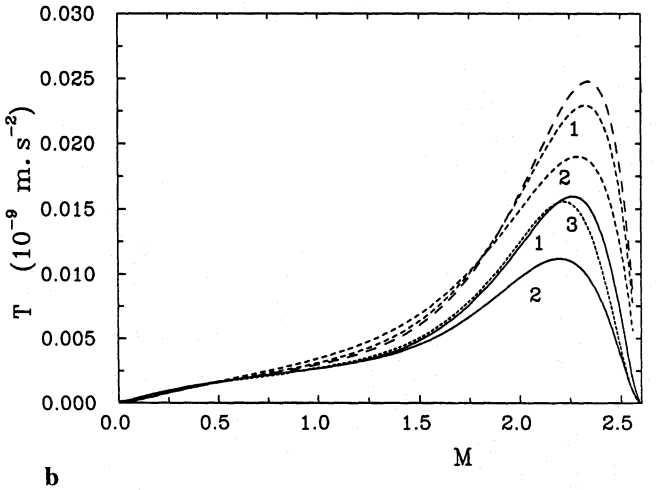

b

Fig. 7a and 7b. The same as in Figs. 6 but for the transverse component T of the radiation pressure acceleration due to specular reflection from the oceans

the exponential model 2, with the narrower distribution for α (curves 1 in parts (b) of Figs. 6 and 7).

The marked decrease in the height of the peaks near sunset (or sunrise) is due to the fact that surface subelements corresponding to lower values of ϑ than the mirror–like value ϑ_0 typically contribute more to the reflected radiation flux than those with $\vartheta > \vartheta_0$, both because lower than mirror–like values of the Fresnel coefficient are preferentially sampled in our statistical model of the reflection geometry, and because the curvature of the Earth's surface results into a solar image in which surface elements with lower than mirror–like reflectivity are the majority (note the shifting position of the mirror–like reflecting point in the solar images shown in Fig. 5). Moreover, when the peak corresponds to case (3), according to the classification of Sect. 3.2, a part of the reflecting $\mathscr{H}$ domain is cut by the terminator of the Earth's cap visible from the satellite. Mathematically, this has the consequence that not all the combinations of the (α, β) parameters in their definition ranges can actually contribute to the reflective radiative field, so that the integral of the probability distribution $\hat{p}(\alpha)$ over the radiative field becomes smaller than 1 (see discussion in Sect. 4).

On the other hand, it is important to note that near their peaks the instantaneous magnitudes of both the perturbing acceleration components are fairly sensitive to the choice of the $\hat{p}(\alpha)$ model and the parameter values adopted in it, implying that more statistical information on the geometry of ocean surfaces would be needed to build a quantitatively accurate model of this perturbation. As for long–term perturbations, they depend on the orbit–averaged values of the force components, and these are likely to be somewhat less sensitive to the reflection models and parameters, since the differences between the various curves are smaller along the rest of the orbit than in the peak regions.

Fig. 6 also shows that the more detailed model produces an artifact in the calculation of the S component near $M = 0$, namely when the satellite's geocentric position vector becomes nearly aligned with the direction of the incoming solar rays. This is due to the fact that the transformation between the (η, ϕ) and the (α, β) angles is no more one–to–one when the domain $\mathscr{H}$ contains the subsatellite point and also the subsolar point [case (1a) described in Sect. 3.2], and becomes really "pathological" when the subsatellite and subsolar points coincide: in this extreme case ($\omega = 0$, occurring at $M = 0$ in our orbital configuration), all the points in the reflecting $\mathscr{H}$ domain have $\beta = -90°$, and since our probability distribution $\hat{p}(\alpha)$ is always uniform with respect to β, the integral in Eq. (24) vanishes. More in general, the average over the ranges of the (η, ϕ) variables for which the radiative field is not zero of the Jacobian appearing in the same integral, weighed with $\hat{p}(\alpha)$, that is

$$P(\omega) = \int_{(\eta,\phi)} d\eta d\phi \, \hat{p}(\alpha) \left| \frac{\partial(\alpha, \beta)}{\partial(\eta, \phi)} \right| , \qquad (26)$$

becomes smaller than unity when the subsatellite and the subsolar points both lie in $\mathscr{H}$ (and vanishes for $\omega = 0$), so that the value of the integral in Eq. (24) is artificially decreased. Thus, in the part of the orbit where this kind of degeneracy occurs, the averaged–$\mathscr{R}$ models provide a more realistic description of the behaviour of the radial force component than the detailed approach based on Eq. (24). On the other hand, note that near $M = 0$ the T component of the perturbing acceleration anyway tends to zero for obvious symmetry reasons, and the comparison between the different models (Fig. 7) shows that no problem arises in this case.

A possible way to remove the "pathological" behaviour described above is simply that of dividing the right–hand side of Eq. (24) by the quantity $P(\omega)$ [Eq. (26)] whenever we are in case (1a) as defined in Sect. 3.2. Since $P(\omega)$ is always equal to unity in cases (1b) and (2), as all combinations of the (α, β) parameters exist in the $\mathscr{H}$ domain and the coordinate transformation $(\eta, \phi) \leftrightarrows (\alpha, \beta)$ is a one–to–one mapping, in these cases our modified version for Eq. (24) would just coincide with the previous one. Note that in case (3) $P(\omega)$ becomes again

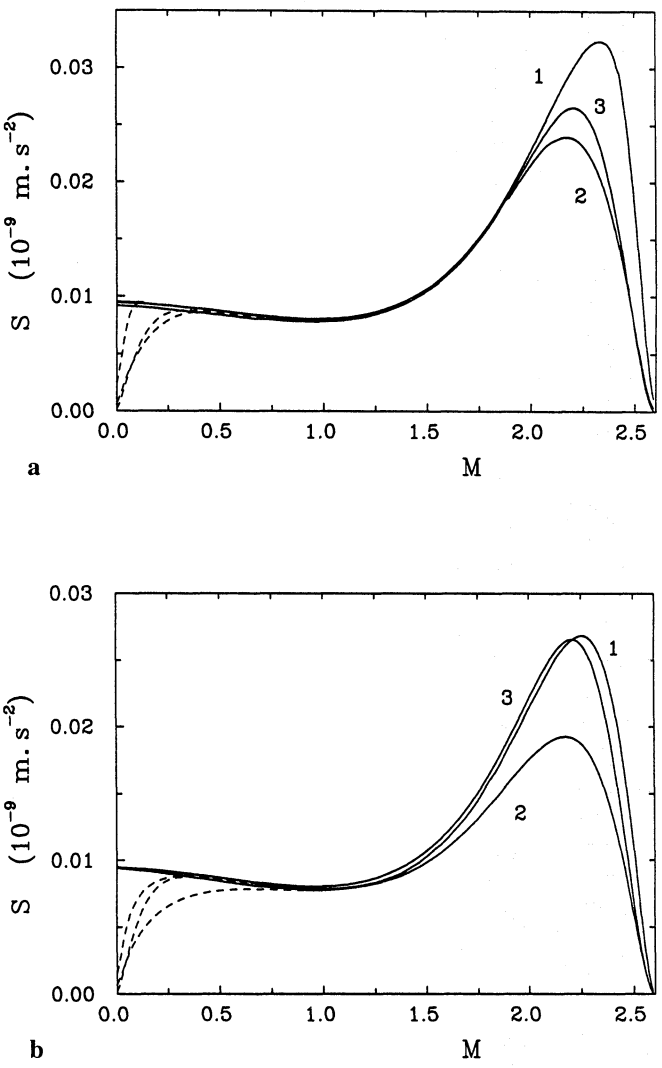

Fig. 8a and 8b. Comparison between the two possible definitions of the reflected–sunlight perturbing acceleration (S component): according to Eq. (24) (dashed curves), and dividing Eq. (24) by the $P(\omega)$ quantity [Eq. (26)] in case (1a), as explained in the text (solid curves). As usual, parts **a** and **b** correspond to models 1,3 and 2,3 for $\hat{p}(\alpha)$, respectively, labels 1 and 2 to different values (5° and 20°) for the input parameters appearing in $\hat{p}(\alpha)$ (models 1 and 2), label 3 in both **a** and **b** to model 3

smaller than unity, but for a different reason: the transformation $(\eta, \phi) \leftrightarrows (\alpha, \beta)$ in this case is still a one–to–one mapping, but the $\mathscr{H}$ domain is cut by the terminator of the Earth's cap visible from the satellite or by the terminator of the illuminated portion of the Earth's surface (see Fig. 5), so the decrease of $P(\omega)$ in case (3) is not an artifact of the statistical method, but just reflects a smaller reflecting domain $\mathscr{H}$.

Figs. 8 show a comparison between the behaviour of the radial S component as predicted by Eq. (24) (dashed curves) and including an additional $1/P(\omega)$ factor (solid curves). It is apparent that the "pathological" drop of S near $M = 0$ disappears in the latter case, and that the corresponding curves become very close to those shown in Figs. 6 for the simpler averaged–$\mathscr{R}$ models. Of course, this way of correcting Eq. (24) in case (1a) is just a heuristic one, and the problem of freeing from "pathological" behaviours statistical models of reflection from a wavy surface such as that discussed in Sect. 3 deserves further study. It is worth mentioning that the models for the T component including the $1/P(\omega)$ factor do not provide any significant changes with respect to the curves shown in Figs. 7, in agreement with our previous remark on this point.

As for the third force component, the binormal one (W, perpendicular to the orbital plane), we recall that its behaviour affects the perturbations on the satellite's orbital inclination and nodal longitude. Therefore estimating its magnitude is important to assess the accuracy achievable in relativistic experiments involving the nodal longitudes of LAGEOS–type satellites (see e.g. Ciufolini 1986, 1987; Ciufolini et al. 1993). As an example, we have derived the W vs. M curve by keeping the same (equatorial) orbit of the satellite, but assuming that the oceans cover only the Southern hemisphere of the Earth, so that no specular reflection occurs from the Northern hemisphere. Thus our hypothetical LAGEOS–type satellite always flies exactly above the ocean/continent boundary. With this configuration, both the simpler approaches discussed earlier (ideal mirror–like reflection or averaged–$\mathscr{R}$ coefficient) would yield a zero binormal component, since a point–like solar image is assumed in them. However, this is not the case for our more detailed model of finite–lobe reflection, as the reflecting part of the ocean in this case is asymmetrical with respect to the (equatorial) plane containing the sun and the orbit.

Fig. 9 shows the resulting values of W vs. M. Here the dashed curves correspond to model 2 for $\hat{p}(\alpha)$, the solid curves to model 1. As usual, labels 1 and 2 correspond to different parameter choices in models 1 and 2, and label 3 to model 3. Note that, as expected, W generally increases for larger aperture angles of the reflection lobe. Also, model 2 yields remarkably higher values of W than model 1, with model 3 in between. This is due to the fact that "misaligned" reflecting elements (with comparatively large α values) contribute most to the binormal component in the peculiar Earth/orbit configuration described above. More general (and realistic) configurations will be explored in a forthcoming study on the long–term perturbations due to reflected sunlight. As in the case of the S component, the drop of all the curves when the "singular" $M = 0$ configuration is approached is a spurious result of our probabilistic algorithm, which could be removed simply by multiplying Eq. (24) by $1/P(\omega)$ in case (1a), as discussed above.

In our last application, we shall test the results reported by Lucchesi & Farinella (1992) concerning the dependence of the orbit–averaged values of the T component (resulting into long–term semimajor axis variations) on the aperture of the reflection lobe. Using a simple reflection model for the finite–cone pattern (a truly axisymmetric cone, whose axis coincides with the ideal specular reflection direction) and an isotropic distribution of the radiation flux inside it, these authors concluded that the dependence on the cone aperture is weak, provided the solid angle spanned by the cone itself is reasonably small (aperture smaller than about 15°). However, in the case of a flux profile

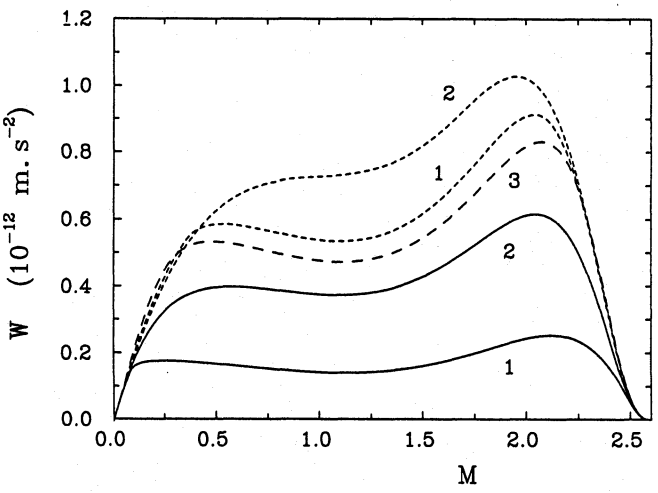

Fig. 9. The binormal component W of the perturbing acceleration due to specular reflection from a Southern–hemisphere ocean vs. mean anomaly M (in radians) for an equatorial LAGEOS–like orbit. The solid and short–dashed curves correspond to models 1 and 2 for $\hat{p}(\alpha)$, respectively, with labels 1 corresponding to $\alpha_\star = 5°$ or $\ln 2/c_2 = 5°$, labels 2 to the value 20° for the same parameters. The long-dashed curve with label 3 corresponds to model 3. The fact that all curves tend to zero when M approaches zero is a spurious result due to the "pathological" behaviour of the probabilistic models, as discussed earlier in the text

decaying exponentially away from the axis of the cone, they found a more pronounced dependence of the results on the cone aperture.

Assessing the extent of this dependence is important, as the "true" aperture of the reflection lobe pattern (or, more plausibly, the typical value of this parameter) is poorly known, and our related parameter choices in models 1 and 2, corresponding to the 5° to 20° range, is just a reasonable guess. Note, however, that none of our models corresponds exactly to the isotropic, axisymmetrical cone pattern of Lucchesi & Farinella, because even in our model 1 the reflection lobe is not symmetrical and the radiative flux inside it is not isotropical (see Sect. 2). Although in line of principle one could search for a probability distribution $\hat{p}(\alpha, \beta)$, necessarily depending also on the β azimuthal angle, such that an isotropic flux distribution would be generated inside a symmetrical reflection cone, this would be anyway a very artificial model. Similar remarks apply to the comparison between our model 2 and the the exponential model of Lucchesi & Farinella, which are similar to each other only in a qualitative way. Therefore, we have chosen just to use models 1 and 2 developed in this paper, by exploiting their parameter dependence to vary in a continuous way the effective aperture of the correponding reflection lobes and compute the resulting orbit–averaged T components.

For these tests we have used the same satellite orbit described earlier and the whole–ocean Earth model; then we have computed the average of the transverse perturbative acceleration component

$$\mathscr{T}(\bar{\alpha}) \equiv \frac{1}{\pi} \int_0^\pi dM\, T\,[M; \alpha_\star, \hat{p}(\alpha)] \ , \tag{27}$$

over the half the orbit (for symmetry reasons, this is the same as the average over the whole orbit), using both models 1 and 2 and changing the parameters specifying the effective aperture of the reflection pattern. Consistently with our previous applications, the argument $\bar{\alpha}$ of $\mathscr{T}$ coincides with $\alpha_\star$ for model 1, whereas for model 2 we define $\bar{\alpha} \equiv \ln 2/c_2$, which characterizes the decay rate of the exponential probability distribution as a function of α. In a semi–quantitative way, $\bar{\alpha}$ is thus related to the aperture of the reflection cone adopted by Lucchesi & Farinella (1992). Note that $\mathscr{T}(\bar{\alpha})$ just corresponds to the integral of the curves represented in Figs. 7 for some specific parameter choices, and that the limiting value of $\mathscr{T}$ for $\bar{\alpha}$ approaching zero provides the resulting averaged T component for the ideal mirror–like reflection case, with no finite–lobe pattern.

Fig. 10 shows the behaviour of $\mathscr{T}(\bar{\alpha})$ vs. $\bar{\alpha}$. Curves 1 and 2 correspond to models 1 and 2 for the probability distribution $\hat{p}(\alpha)$, respectively. In both cases we observe a decrease of the resulting value of $\mathscr{T}$ when $\bar{\alpha}$ increases. For small values of $\bar{\alpha}$ this dependence is weaker for model 1 than for model 2, in agreement with the results of Lucchesi & Farinella. However, the opposite is true for $\bar{\alpha}$ larger than about 10°. The range of $\mathscr{T}$ values — from about 2 to 3.3×10^{-12} m/s^2 — is also close to that estimated in previous studies, with a maximum excursion of the order of 40% between the results of different models and parameter choices. Note that with a more realistic model for the Earth's surface (partially covered by continents and clouds) the resulting value of $\mathscr{T}$ would be decreased by a further factor of the order of 2. Thus it appears likely that this perturbation provides a significant but not dominant contribution to the observed long–periodic variations of LAGEOS' semimajor axis, which correspond to orbit–averaged along–track accelerations of $\approx 3 \times 10^{-12}$ m/s^2. We shall address this problem in more detail in a forthcoming paper.

5. Conclusions

The main results of this paper can be summarized as follows:

1. We have developed a realistic theory of specular reflection from a wavy ocean surface, taking into account the finite–lobe effects through a statistical model for the orientation of the small–scale surface elements. Two different modelling methods have been tested: (i) that of keeping the ideal, mirror–like reflection geometry from a single point on the surface, but replacing the ideal Fresnel reflection coefficient for an air/water boundary with an "effective" coefficient, averaged over all the possible orientations of the infinitesimal reflecting surfaces (Sect. 2); (ii) a more detailed treatment of the reflection geometry for different light rays coming from an extended region of the Earth's surface. We have derived the corresponding expressions for the radiation pressure perturbative acceleration, and carried out some comparisons changing the position of a fictitious LAGEOS–type satellite

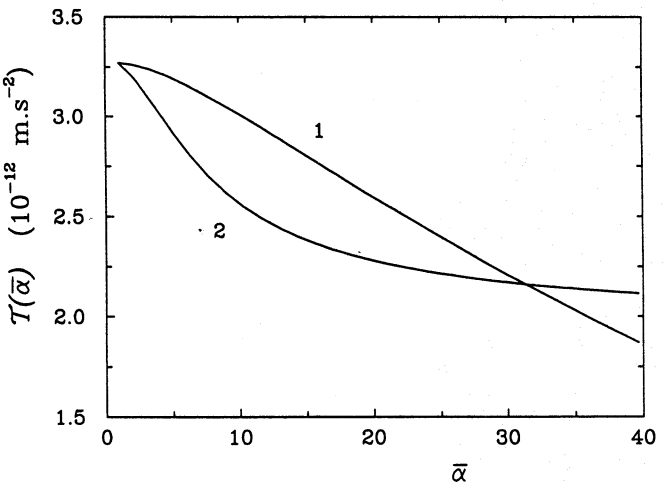

Fig. 10. The orbit–averaged transverse component $\mathcal{T}$ vs. the effective aperture $\bar{\alpha}$ (in degrees) of the reflection lobe pattern for models 1 and 2 of $\hat{p}(\alpha)$ (the curve labels indicate the corresponding models)

along its orbit. The results clearly show that significant differences are caused by different modelling choices. A forthcoming study will be devoted to study the corresponding long–term perturbations and the optimal modelling strategies for the analysis of real tracking data [note that the simpler method (i) entails much shorter computing times than the more realistic method (ii)].

2. We confirm that finite–lobe phenomena may have caused some inaccuracy in the results of previous studies on the albedo effect on LAGEOS (as suggested to us by V. Slabinski, 1993, personal communication). This probably entails an overestimate of the perturbing force (and of its orbit–averaged transverse force component) ranging from $\approx 10\%$ to 40%, depending on the details of the adopted model for the statistical distribution of the orientation of the small—scale reflecting surface elements. A model based on aerial photographic data of the sun's glitter from the sea surface (Cox & Munk 1954) gives results qualitatively similar to those of simpler mathematical models, and corresponding to moderate values of the parameters describing the typical sea surface "roughness". In general, the orbit–averaged T component somewhat decreases when this "roughness" and the corresponding aperture of the reflection lobe are assumed to grow.
3. An estimate based on the results shown in Fig. 9 would lead to conclude that the LAGEOS/LAGEOS3 combined nodal motion due to the out–of–plane perturbing acceleration W from oceanic specular reflection (and its finite–lobe pattern) is small enough not to compete with the general–relativistic orbit precession whose measurement is the main purpose of this planned mission. If the amplitude of the average out–of–plane acceleration is of the order $10^{-12}\,\mathrm{m/s^2}$, this corresponds to a nodal precession rate the order of 10^{-3} arcsec per year, that is just a few percent of the Lense–Thirring effect. However, our assumed ocean/continent distribution and orbit geometry are very artificial, so more realistic models are needed to obtain better estimates of this effect. It appears likely that such models will lead to even smaller values of the orbit–averaged W component, since the real orbit seldom overflies a coastal line, and even when it does, configurations resulting into W contributions with opposite signs are about equally lileky during each revolution.
4. We have checked the results reported by Lucchesi & Farinella (1992) on the dependence of the orbit–averaged transverse component of the reflected–sunlight perturbing acceleration on the aperture of the reflection cone pattern. For all our model choices, we have observed a moderate dependence of the results on this parameter, somewhat more pronounced for model 2 [exponential decrease of the probability distribution $\hat{p}(\alpha)$], in close similarity to the results reported by Lucchesi & Farinella. In a forthcoming paper, we will try to assess in a quantitative way the role of specularly reflected radiation in generating the LAGEOS semimajor axis residuals.

Acknowledgements. We are grateful to V.J. Slabinski for having suggested to us to undertake this work, and to G. Caudal for calling our attention to the measurements of Cox & Munk (1954) and the corresponding empirical model for the roughness of the sea surface. We also thank B. Chauvineau for help in producing the figures. D.V.'s work was partially supported by the IBM Academic Initiative in the Czech Republic and by an EEC grant to stay at the Observatoire de la Côte d'Azur (OCA, Dept. CERGA, Grasse, France) in the summer of 1993. P.F. worked to this project while staying at OCA (Dept. Cassini, Nice, France) thanks to the "G. Colombo" fellowship of the European Space Agency.

References

Antreasian, P.G., 1992, Precision radiation force modeling for the TOPEX/POSEIDON mission, Ph.D. Thesis, University of Colorado

Anselmo L., Farinella P., Milani A., Nobili A.M., 1983, A&A 117, 3

Baker R.M.L., 1963, Radiation on a satellite in the presence of partly diffuse and partly specular reflecting body, In: M. Roy (ed.) Dynamics of Satellites. Springer–Verlag, Berlin, p. 85

Bass F.G., Fuks I.M., 1979, Wave Scattering from Statistically Rough Surfaces, Pergamon Press, Oxford

Barlier F., Carpino M., Farinella P., Mignard F., Milani A., Nobili A.M., 1986, Ann. Geophys. 4, 193

Borderies N., Longaretti P.-Y., 1990, Celest. Mech. 49, 69

Ciufolini I., 1986, Phys. Rev. Lett. 56, 278

Ciufolini I., 1987, Celest. Mech. 40, 19

Ciufolini I., Farinella P., Nobili A.M., Lucchesi D., Anselmo L., 1993, Nuovo Cimento 108 B, 151

Cox C., Munk W., 1954, J. Opt. Soc. of America 44, 838

Fliegel H.F., Gallini T.E., Swift E.R., 1992, J. Geophys. Res. 97, 559

Hennings I., Matthews, J., Metzner, M., 1994, J. Geophys. Res. 99, 16303

Jackson J.D., 1962, Classical Electrodynamics, Wiley & Sons, New York

Klinkrad H., Koeck Ch., Renard P., 1990, ESA Journal 14, 409

Levin E., 1962, ARS Journal, 1328

Lucchesi D., Farinella P., 1992, J. Geophys. Res. 97, 7121

Mignard F., Afonso G., Barlier F., Carpino M., Farinella P., Milani A., Nobili A..M., 1990, Adv. Space Res. (3)221
Mihalas D., 1970, Stellar Atmospheres, Freeman and Co., San Francisco
Milani A., Nobili A..M., Farinella P., 1987, Non–Gravitational Perturbations and Satellite Geodesy, Hilger, Bristol
Peřestý R., Sehnal L., 1992, In–orbit microaccerelerometric experiment, presented at the 43rd congress of the International Astronautical Federation, Washington DC
Rubincam D.P., Weiss N.R., 1986, Celest. Mech. 38, 233
Rubincam D.P., Knocke P., Taylor V.R., Blackwell S., 1987, J. Geophys. Res. 92, 11,662
Stratton J.A., 1941, Electromagnetic Theory, McGraw–Hill, New York
Taylor V.R., Stowe L.L., 1984, J. Geophys. Res. 89, 4987
Vilhena de Moraes R., 1994, Adv. Space Res. 14, (5)45
Vokrouhlický D., 1994, Radiation force model for CESAR experiment, Publ. Astron. Inst. Ondřejov 82, 15
Vokrouhlický D., Sehnal L., 1993, Celest. Mech. 57, 493
Vokrouhlický D., Farinella P., Lucchesi D., 1993a, Celest. Mech. 57, 225
Vokrouhlický D., Farinella P., Lucchesi D., 1993b, A&A 280, 282
Vokrouhlický D., Farinella P., Mignard F., 1993c, A&A 280, 295
Vokrouhlický D., Farinella P., Mignard F., 1994, A&A 290, 324
Wentz F.J., Peteherych S., Thomas L.A., 1984, J. Geophys. Res. 89, 3689
Wyatt S.P., 1963, The effect of terrestrial radiation pressure on satellite orbits, in: M. Roy (ed.), Dynamics of Satellites, Springer–Verlag, Berlin, p. 180

This article was processed by the author using Springer-Verlag TEX A&A macro package 1992.